Morphological Cell Profiling of SARS-CoV-2 Infection Identifies Drug Repurposing Candidates for COVID-19

Carmen Mirabelli[1,*], Jesse W. Wotring[2,*], Charles J. Zhang[2,†], Sean M. McCarty[2,†], Reid Fursmidt[3,4,†], Tristan Frum[5,] Namrata S. Kadambi[3], Anya T. Amin[3], Teresa R. O'Meara[1], Carla D. Pretto[1], Jason R. Spence[3,5], Jessie Huang[6,7], Konstantinos D. Alysandratos[6,7], Darrell N. Kotton[6,7], Samuel K. Handelman[3,4], Christiane E. Wobus[1], Kevin J. Weatherwax[4,8,9], George A. Mashour[4,8,10], Matthew J. O'Meara[11‡], Jonathan Z. Sexton[2,3,4,8‡]

[1]Department of Microbiology and Immunology, University of Michigan Medical School, Ann Arbor, MI, 48109, USA
[2]Department of Medicinal Chemistry, College of Pharmacy, University of Michigan, Ann Arbor, MI, 48109, USA
[3]Department of Internal Medicine, Gastroenterology, Michigan Medicine at the University of Michigan, Ann Arbor, MI, 48109, USA
[4]U-M Center for Drug Repurposing, University of Michigan, Ann Arbor, MI, 48109, USA
[5]Department of Cell and Developmental Biology, University of Michigan, Ann Arbor, MI, 48109, USA
[6]Center for Regenerative Medicine of Boston University and Boston Medical Center, Boston, MA, 02118, USA
[7]The Pulmonary Center and Department of Medicine, Boston University School of Medicine, Boston, MA, 02118, USA
[8]Michigan Institute for Clinical and Health Research (MICHR), University of Michigan, Ann Arbor, MI, 48109, USA
[9]College of Pharmacy, University of Michigan, Ann Arbor, MI 48109, USA
[10]Department of Anesthesiology, Michigan Medicine at the University of Michigan, Ann Arbor, MI, 48109, USA
[11]Department of Computational Medicine and Bioinformatics, University of Michigan, Ann Arbor, MI, 48109, USA

[*]These authors contributed equally to this work.
[†]These authors contributed equally to this work.
[‡]Co-Senior Authors

Abbreviations:

MOI: multiplicity of infection
UMAP: uniform manifold approximation and projection
COVID-19: Coronavirus Disease-2019
MOA: mechanism of action
ROI: region of interest
iAEC2: induced pluripotent stem cell (iPSC)-derived alveolar epithelial type 2 cells
HCQ: hydroxychloroquine

Conflicts of interest

The authors declare no conflicts of interest.

ABSTRACT

The global spread of the severe acute respiratory syndrome coronavirus 2 (SARS-CoV-2), and the associated disease COVID-19, requires therapeutic interventions that can be rapidly identified and translated to clinical care. Unfortunately, traditional drug discovery methods have a >90% failure rate and can take 10-15 years from target identification to clinical use. In contrast, drug repurposing can significantly accelerate translation. We developed a quantitative high-throughput screen to identify efficacious single agents and combination therapies against SARS-CoV-2. Quantitative high-content morphological profiling was coupled with an AI-based machine learning strategy to classify features of cells for infection and stress. From a library of 1,425 FDA-approved compounds and clinical candidates, we identified 17 dose-responsive compounds with antiviral efficacy. In particular, we discovered that lactoferrin is an effective inhibitor of SARS-CoV-2 infection with an IC_{50} of 308 nM and that it potentiates the efficacy of both remdesivir and hydroxychloroquine. Lactoferrin also stimulates an antiviral host cell response and retains inhibitory activity in iPSC-derived alveolar epithelial cells, a model for the primary site of infection. Given its safety profile in humans, these data suggest that lactoferrin is a readily translatable therapeutic option for COVID-19. Additionally, several commonly prescribed drugs were found to exacerbate viral infection and warrant follow up studies. We conclude that morphological profiling for drug repurposing is an effective strategy for the selection and optimization of drugs and drug combinations as viable therapeutic options for COVID-19 pandemic and other emerging infectious diseases.

65 **MAIN**

66 SARS-CoV-2 is an enveloped, positive-sense, single-stranded RNA betacoronavirus that
67 emerged in Wuhan, China in November 2019 and rapidly developed into a global pandemic. The
68 associated disease, COVID-19, has an array of symptoms, ranging from flu-like illness and
69 gastrointestinal distress[1,2] to acute respiratory distress syndrome, heart arrhythmias, strokes, and
70 death[3,4]. Drug repurposing has played an important role in the search for COVID-19 therapies.
71 Recently, the FDA issued emergency approval of remdesivir, a nucleoside inhibitor prodrug
72 developed for Ebola virus treatment[5], and hydroxychloroquine, an aminoquinoline derivative first
73 developed in the 1940s for the treatment of malaria, for patients with severe COVID-19. However,
74 there are no established prophylactic strategies or direct antiviral treatments available to limit
75 SARS-CoV-2 infections and to prevent/cure the associated disease COVID-19.

76

77 Repurposing of FDA-approved drugs is a promising strategy for identifying rapidly deployable
78 treatments for COVID-19. Benefits of repurposing include known safety profiles, robust supply
79 chains, and a short time-frame necessary for development[6]. Additionally, approved drugs serve
80 as chemical probes to understand the biology of viral infection and can help make new
81 associations between COVID-19 and molecular targets/pathways that influence pathogenesis of
82 the disease. A complementary approach to standard *in vitro* antiviral assays is high-content
83 imaging-based morphological cell profiling. Using morphological cell profiling, it is possible to
84 identify pathways and molecular targets underlying infection, thus allowing for targeted screening
85 around a biological process or targeting of host processes that limit viral infection.

86 Here, we developed a pipeline for quantitative high-throughput image-based screening of SARS-
87 CoV-2 infection. We leveraged machine learning approaches to create an assay metric that
88 accurately and robustly identifies features that predict antiviral efficacy. From this, we identified

89 several FDA-approved drugs and clinical candidates with unique antiviral activity. We further
90 demonstrated that one of our most promising hits, lactoferrin, inhibits viral entry and replication,
91 enhances antiviral host cell response, and potentiates the effects of remdesivir and
92 hydroxychloroquine. Furthermore, we identified currently prescribed drugs that exacerbate viral
93 infectivity. As a confirmatory step, efficacy of lead drugs was validated in a highly physiologically
94 relevant organotypic and biomimetic human model system for bronchial epithelium. Collectively,
95 we present evidence that morphological profiling can be used to characterize the viral life cycle in
96 vitro and robustly identify new potential therapeutics against SARS-CoV-2 infection.

97

98 **Morphological profiling reveals unique features associated with SARS-CoV-2 infection**

99 To determine the optimal cell line and appropriate endpoint for antiviral drug screening, we
100 assessed SARS-CoV-2 infectivity in previously reported permissive cell lines: Vero E6, Caco-2,
101 and Huh7[7]. Viral growth kinetics at a multiplicity of infection (MOI) of 0.2 revealed that Vero E6,
102 Caco-2, and Huh7 cells supported viral infection, with peak viral titers at 48 hours post infection
103 (hrs p.i.) (Supplementary Figure 1a/b). Although the viral load was higher in Vero E6 cells, Huh7
104 were selected for our morphological drug screen as a human cell line that expresses both ACE2
105 and TMPRSS2, which are the primary entry factors for SARS-CoV-2[8]. Infection was detectable in
106 Huh7 cells at an MOI as low as 0.004 at 48 hrs p.i. (Supplementary Figure 1c), which highlights
107 the high sensitivity of image-based screening. To identify compounds that inhibit or exacerbate
108 infection, we selected an MOI of 0.2, leading to a baseline infectivity rate of 20%.

109 Morphological cell profiling was enabled through multiplexed staining and automated high-content
110 fluorescence microscopy. Our multiplexed dye set included markers for SARS-CoV-2
111 nucleocapsid protein (NP), nuclei (Hoechst 33342), neutral lipids (HCS LipidTox Green), and cell
112 boundaries (HCS CellMask Orange). These fluorescent probes were chosen to capture a wide

113 variety of cellular features relevant to viral infectivity, including nuclear morphology, nuclear
114 texture, cytoplasmic and cytoskeletal features, and indicators of cell health.

115 We observed several prominent features associated with SARS-CoV-2 infection in Huh7 cells
116 including: the formation of syncytia, small/round cells with a prominent negative viral staining in
117 the nucleus, increased nucleoli count (Supplementary Figure 1d), and cytoplasmic protrusions
118 (Figure 1a). These protrusions are consistent with what has been observed in other cell lines
119 infected with SARS-CoV-2, including Vero-E6 and Caco-2.[9]

120 In order to quantify the unique morphological features associated with viral infection in Huh7 cells,
121 we used the image segmentation and analysis software CellProfiler to measure 660 cellular
122 features on a per-cell basis. Features included measurements of intensity, radial distribution, and
123 texture for each fluorescent channel.[10] Infected cells were initially distinguished from uninfected
124 cells by the presence of NP signal, however through morphological profiling we determined that
125 there were several different manifestations of the infection within the cell population.

126 The different stages of infection are described by their divergence of intensity and morphological
127 features in any of the fluorescent channels. To efficiently display the diversity of natural
128 morphologies of infected cells, cellular features were dimensionally reduced via the non-linear
129 uniform manifold approximation and projection (UMAP) to embed 2.47 million infected cells into
130 2-dimensions. Clusters of cells were identified based on isolated clusters or regional high-density
131 peaks[11] (Figure 1b, Supplementary Figure 2). In the UMAP embedding, we identified 12 regions
132 of interest (ROI) with high cell density. Inspection of cell images within ROIs revealed distinct
133 morphologic characteristics that include punctate NP signal (ROI 11), individually infected cells
134 with high NP intensity at the periphery (ROI 9), cells in multinucleated syncytia (ROI 8) and
135 infected cells with protrusions wrapping around uninfected cells (ROI 6). Inhibition of viral
136 progression is the aim for antiviral therapeutics, therefore compounds that impede any of these

137 phenotypic stages can potentially be useful for treatment of SARS-CoV-2 infection. To leverage
138 the spatial resolution of imaging-based screening, we used a multivariate scoring system that
139 incorporated both intensity and morphometric measurements to determine antiviral efficacy rather
140 than single measurements based on viral staining intensity or rescuing a cytopathic effect.
141 Phenotypic features describing the different stages of infection in Huh7 cells were used to
142 generate a machine learning pipeline for antiviral drug screening

143 **Machine learning identifies FDA-approved molecules with antiviral activity against SARS-**
144 **CoV-2**

145 To identify compounds with antiviral activity against SARS-CoV-2, we screened a library of 1,425
146 FDA-approved compounds and rationally included clinical candidates (Supplementary File 1) in
147 quantitative high-throughput screening (qHTS) at five concentrations (50 nM, 250 nM, 500 nM,
148 1000 nM and 2000 nM) in Huh7 cells. Compounds were assessed for their antiviral activity using
149 a CellProfiler-based image analysis pipeline and a random forest classification algorithm to
150 identify infected cells and quantify their morphological characteristics (Figure 2a). The random
151 forest classifier leveraged 660 unique cellular features including measurements of intensity,
152 texture and radial distribution for each fluorescent channel (nuclei, cytoplasm, lipid, virus). From
153 the qHTS, 132 drugs were selected as active with consistent decreases in viral infectivity in at
154 least three of the tested concentrations as well as minimal cytotoxicity.

155

156 In confirmatory screening, 10-point, two-fold dilution dose-response experiments were performed
157 in triplicate on the 132 qHTS hits, with validation of dose-responsive efficacy for 17 compounds
158 below 1 μM potency (Supplementary Table 1 and Figure 2b). These hits include eleven that are
159 novel *in vitro* observations (bosutinib, domperidone, entecavir, fedratinib, ipratropium bromide,
160 lacoferrin, lomitapide, metoclopramide, S1RA, thioguanine, and Z-FA-FMK), and six that have

161 been previously identified to have antiviral activity (amiodarone, verapamil, gilteritinib,
162 clofazimine[12,13], niclosamide[14], and remdesivir). Amiodarone, gilterinib, lomitapide, thioguanidine
163 and Z-FA-FMK retained activity in a traditional CPE-based antiviral assay in Vero E6
164 (Supplementary Table 1). In addition to antiviral drug hits, we also identified several compounds
165 that appear to exacerbate SARS-CoV-2 infection, including trametinib, binimetinib and
166 cobimetinib -potent MEK inhibitors used to treat metastatic melanoma- and the Parkinson's
167 disease drugs carbidopa, methyldopa and levodopa (Supplementary Figure 3).
168

169 **Lactoferrin blocks SARS-CoV-2 replication at different stages of the viral cycle**

170 One of the most efficacious hits identified from our screen was lactoferrin, a protein found in milk
171 and other secretory fluids[15]. We determined that lactoferrin has dose-dependent antiviral activity
172 through a range of MOIs (Figure 3a and b). Previous work on lactoferrin in the context of infection
173 with SARS-CoV-1 suggests that it blocks viral entry by binding heparan sulfate proteoglycans that
174 are important for early viral attachment[16]. Lactoferrin blocks SARS-CoV-2 infection via entry
175 inhibition (Supplementary Figure 4) and also has significant antiviral activity when added 1 or 24
176 hrs p.i. (Figure 3b), suggesting multimodal efficacy. Lactoferrin has been proposed to enhance
177 innate interferon responses to limit viral replication within host cells[17]. Upon treatment, we
178 observed a dose-dependent reduction of viral replication (Figure 3c), which was consistent with
179 elevated mRNA levels of IFNβ and interferon-stimulated genes (ISG15, MX1, Viperin and IFITM3)
180 in lactoferrin-treated Huh7 cells (Figure 3d). Interestingly, we detected a robust antiviral effect by
181 both holo and apolactoferrin (human and bovine), the latter being the component of widely
182 available dietary supplements. To rule out a mode of action that involved a general iron depletion
183 mechanism, we tested the protein transferrin and found that it was devoid of any anti-SARS-CoV-
184 2 activity at the highest concentration of 2.3 μM (Figure 3e).

185

186 A clinically effective strategy for antiviral therapies uses a combinatorial (or “drug cocktail”)
187 approach, where compounds with varying mechanisms of action are concomitantly used to target
188 different stages in the viral life cycle and to minimize the risk of acquired drug resistance from
189 single-agent selective pressure. This is especially true for RNA viruses, which are highly variable
190 and can develop drug-resistance[18]. Given the pronounced single-agent efficacy of lactoferrin, we
191 tested whether combinations with remdesivir or hydroxycholoroquine could improve the overall
192 antiviral activity. We found that lactoferrin potentiates the efficacy of both remdesivir (Figure 3f
193 and Supplementary Figure 5a) and hydroxychloroquine (Figure 3f and Supplementary Figure 5b),
194 which are currently explored treatments for SARS-CoV-2 infection. Therefore, combination
195 therapy with lactoferrin could be beneficial in the management of the COVID-19 pandemic by
196 reducing toxicity (e.g., hydroxycholorquine) or consumption (e.g., remdesivir).
197
198

199 **Lead compounds demonstrate efficacy in iPSC-derived model of bronchial epithelium**

200 To evaluate the translatability of our identified lead compounds, we used a biomimetic model of
201 bronchial epithelium, iPSC-derived alveolar epithelial type 2 cells (iAEC2s)[19]. Surfactant protein
202 C positive (SFTPC+) epithelial cells were previously used to model other lung diseases in place
203 of primary AEC2s[20]. The advantage of using iPSC-derived AEC2s is in the development of
204 physiologically relevant heterogeneous airway cell populations that includes alveolar type II cells,
205 that are involved in COVID-19 pathogenesis[21]. We demonstrated that iAECs are permissive to
206 infection with an MOI of 10, resulting in 50-60% infected cells. Acetylated tubulin staining revealed
207 variable cytoskeleton structures, reminiscent of different cell types, and interesting protrusions
208 that co-stained with viral NP-protein. The morphology of infected cells has key differences
209 compared to the other cell types used in our study; particularly, the proportion of individually
210 infected cells are greater than viral syncytia (Figure 4b). Remarkably, even at a high MOI of 10,

211 dose-responsive antiviral activity was observed with bovine lactoferrin (IC_{50} = 45 nM), human
212 lactoferrin (IC_{50} = 466 nM), S1RA (IC_{50} = 1 μM), and remdesivir (IC_{50} = 18 nM) (Figure 4a). At lower
213 MOIs, the infection rate in iAEC2s was more variable. However, with a lower MOI of 0.2 the dose
214 dependent antiviral efficacy was observed for amiodarone, lomitapide, ipratropium bromide,
215 clofazimine, gilteritinib and fedratinib (Supplementary Figure 6). This physiologically relevant
216 model is a proxy of human lung tissue and serves as an intermediate model to further validate
217 clinical potential of our identified lead compounds prior to *in vivo* studies.

218

219 **DISCUSSION**

220 In this study, we developed an experimental workflow based on high-content imaging and
221 morphological profiling that allows for rapid screening of FDA-approved compounds, leveraging
222 machine learning to score compounds based on many different cellular features relevant to
223 infection. Our morphological profiling analysis and corresponding UMAP embedding
224 demonstrated that SARS-CoV-2 infection in Huh7 cells is variable and highlights the necessity of
225 multivariate scoring systems to assess efficacy. From our SARS-CoV-2 screening, we identified
226 17 FDA-approved compounds that limit infection *in vitro*. Of these, six were previously reported
227 and serve as a benchmark validation of our endpoints and experimental approach, and eleven
228 were hitherto unknown. We demonstrate that this approach is versatile (i.e., it can be applied to
229 both transformed and more physiologically-relevant non-transformed cell lines) and can identify
230 the emergent properties of the infection as well as novel phenotypes that can be perturbed
231 through chemical inhibition.

232 Importantly, our study identified drugs that implicate new molecular targets/pathways in the
233 pathogenesis of SARS-CoV-2 and produce clinically testable and readily translatable hypotheses.
234 As an example, we observed dose-dependent antiviral activities of metoclopramide and

235 domperidone, two potent dopamine receptor D2 antagonists used to treat gastroesophageal
236 reflux disease and prevent other gastrointestinal symptoms, including nausea and vomiting[22].
237 Gastrointestinal symptoms have been increasingly reported in more than half of the patients
238 infected by SARS-CoV-2[2]. Notably, investigational drugs like hydroxychloroquine, lopinavir-
239 ritonavir, tocilizumab and others can be associated with gastrointestinal and hepatic adverse
240 events and hence are not ideal for patients already experiencing severe GI symptoms[23].
241 Metoclopramide and domperidone therefore represent a dual-target therapeutic option for
242 COVID-19 patients. In contrast, the pro-dopaminergic drugs carbidopa, levodopa, and
243 methyldopa promote infection, suggesting that the dopamine pathway may contribute to adverse
244 infection outcomes. Additionally, all FDA-approved MEK inhibitors exacerbate viral infection 3-
245 fold indicating a putative role of MEK in SARS-CoV-2 pathogenesis. These *in vitro* observations
246 should be validated through clinical research that examines whether concomitant presence of
247 drug and SARS-CoV-2 infection worsen COVID-19 symptoms.

248 As most FDA-approved drugs are optimized against human molecular targets, our screen helped
249 identify crucial host factors involved in SARS-CoV-2 infection. Z-FA-FMK, an irreversible inhibitor
250 of cysteine proteases, including cathepsins B, L, and S[24], exhibited potent antiviral activity. A
251 recent report using a pseudovirus indicated cathepsin L is an entry factor of SARS-CoV-2[25]. The
252 antiviral effect of Z-FA-FMK suggests that cathepsin L is a requirement also in the context of
253 SARS-CoV-2 infection and suggests that this molecule could be a useful investigational tool to
254 study virus entry. Similarly, fedratinib, approved by the FDA in 2019 for myeloproliferative
255 neoplasms[26], is an orally bioavailable semi-selective JAK2 inhibitor. JAK-inhibitors have been
256 proposed for COVID-19 to specifically inhibit TH17-mediated inflammatory responses. JAK-
257 inhibitors have been proposed for COVID-19 treatment to specifically inhibit TH17-mediated
258 inflammatory response[27,28] and to block numb-associated kinase responsible for clathrin-
259 mediated viral endocytosis[29]. Several JAK-inhibitors are currently evaluated in clinical trials for

260 COVID-19 management, including with baricitinib[30], jakotinib (ChiCTR2000030170), and
261 ruxolitinib (ChiCTR2000029580). For their inhibitory effect on innate immune response at the
262 cellular level, JAK-inhibitors could serve as useful tools in the future to elucidate the involvement
263 of the innate immune response in SARS-CoV-2 infection.

264

265 The sigma receptors (SigmaR1/R2) are permissive chaperones that mediate endoplasmic
266 reticulum stress response and lipid homeostasis[31], processes that have been implicated in early
267 stages of hepatitis C viral infection in Huh7 cells[32] and coronavirus pathogenesis[33]. We identified
268 two sigma receptor modulators amiodarone[34], and S1RA[35] with potent antiviral activity,
269 demonstrating IC_{50} values of 52 nM and 222 nM, respectively, with limited cell toxicity. Amiodarone
270 is approved for treatment of arrhythmias but, like hydroxychloroquine, has potent cardiotoxic side
271 effects through inhibition of the hERG ion channel[36] that limit therapeutic potential. S1RA has
272 completed phase II clinical trials for the treatment of neuropathic pain[37,38]. Although Gordon *et al.*
273 identified several other sigmaR1/R2 modulators that inhibited SARS-CoV-2 infection in Vero-E6
274 cells, antiviral activity for S1RA was not observed[9]. This suggests that the activity of S1RA is
275 dependent on host cell factors specific to each cell line and, promisingly, that human cells may
276 be more responsive to this compound, as observed in iAEC2s (Figure 5a).

277

278 Most noteworthy, our screen demonstrates lactoferrin as a SARS-CoV-2 inhibitor *in vitro* with
279 multimodal efficacy. We showed that lactoferrin strongly inhibits cellular binding of SARS-CoV-2
280 and is therefore a promising therapy for pre- and post-exposure prophylaxis. We also showed
281 dose-dependent efficacy in multiple cell types, including a non-transformed and clinically relevant
282 iPSC-derived model of alveolar epithelium. Lactoferrin gene expression has been shown
283 previously to be highly upregulated in response to SARS-CoV-1 infection[39] and, in addition to

284 enhancing natural killer cell and neutrophil activity, lactoferrin blocks viral entry through binding
285 to heparan sulfate proteoglycans. Lactoferrin retains anti-SARS-CoV-2 activity 24 hrs p.i., which
286 suggests additional MOA other than simple entry inhibition. Although we cannot conclude a
287 definitive and complete MOA, we show significant host cell modulation through increased
288 expression of several interferon-stimulated genes upon treatment with lactoferrin. Additionally,
289 lactoferrin has been previously shown to decrease the production of IL-6[40], which is one of the
290 key players of the "cytokine storm" produced by SARS-CoV-2 infection[41,42]. We found that
291 lactoferrin, either from bovine or human origin, retain activity in both the holo- and apo- forms, the
292 latter being the component of orally available lactoferrin supplements. Lactoferrin potential is
293 heightened by its ability to mitigate a high MOI SARS-CoV-2 infection in iAEC2 (Figure 5). Orally
294 available lactoferrin could be especially effective in resolving the gastrointestinal symptoms that
295 are present in COVID-19 patients[43]. The mechanisms may be similar to how lactoferrin reduces
296 human norovirus infection through induction of innate immune responses[44], especially as
297 lactoferrin gene polymorphisms are associated with increased susceptibility to infectious
298 diarrhea[45]. If lactoferrin reduces viral load in the GI tract, it could reduce fecal-oral transmission
299 of COVID-19[46].

300 Combination therapies are likely to be required for effectively treating SARS-CoV-2 infection, and
301 this approach has already shown promise. For example, combination therapy with interferon beta-
302 1b, lopinavir–ritonavir, and ribavirin showed efficacy against SARS-CoV-2 in a prospective, open-
303 label, randomized, phase 2 trial[47]. We show that lactoferrin potentiates the antiviral activity of both
304 remdesivir and hydroxychloroquine and could be used as a combination therapy with these drugs,
305 which are currently being used or studied for the treatment of COVID-19. Due to its wide
306 availability, limited cost, and lack of adverse effects, lactoferrin could be a rapidly deployable
307 option for both prophylaxis and the management of COVID-19. Likewise, ipratropium bromide, a
308 widely-used quaternary ammonium salt bronchodilator, holds promise as another agent for

309 combination therapies with potential to reduce bronchial viral burden. Although our findings are
310 promising, further studies are needed to confirm the efficacy of our lead antiviral compounds in
311 other representative *in vitro* cell lines and/or clinical studies.

312 High-content morphological cell profiling for drug repurposing screening enabled the identification
313 of both novel antivirals efficacious against SARS-CoV-2 and compounds that possibly exacerbate
314 SARS-CoV-2 infection. Confirmation in iAEC2s suggests high clinical translatability of these
315 compounds. This approach to preclinical testing has promise for identifying other anti-SARS-CoV-
316 2 drugs, rationally designing therapeutic combinations with multiple MOAs, and deployment of
317 optimized combinations in a rapid and systemic fashion.

318

319 Supplementary Information is available for this paper.

320

321 Correspondence and requests for materials should be addressed to jzsexton@umich.edu

322

323

324

325

326

327
328
329

330

ACKNOWLEDGEMENTS

Funding: University of Michigan Institute for Clinical and Health Research (MICHR) (NCATS - UL1TR002240) and its Center for Drug Repurposing. JZS is supported by the National Institute of Diabetes and Digestive and Kidney Diseases (R01DK120623). JWW is supported by the pharmacological sciences training program (PSTP) T32 training grant. CM is supported by Marie-Slodowska Curie individual fellowship (GA - 841247) and MICHR Postdoctoral Translational Scholars Program. KDA is supported by the I.M. Rosenzweig Junior Investigator Award from the Pulmonary Fibrosis Foundation. JRS is supported by the National Heart, Lung, and Blood Institute (NHLBI – R01HL119215), by the NIAID Novel Alternative Model Systems for Enteric Diseases (NAMSED) consortium (U19AI116482) and by grant number CZF2019-002440 from the Chan Zuckerberg Initiative DAF, an advised fund of Silicon Valley Community Foundation.

The authors would like to thank Matthew Chess for Amazon AWS support, Kevin Jan and Peyton Uhl at Yokogawa for imaging support, Nick Santoro at the University of Michigan Center for Chemical Genomics. We thank David Egan and Wienand Omta from Core Life Analytics for assisting high content data analytics as well as Philip Cheung and Brian Bolt at ReFactor Biosciences for assistance with HTS data registration. Finally, we thank Tracey Schultz and Dianne Jazdzyk for project management.

METHODS

Cells and virus. Vero E6, Caco-2 and Huh7 cells were maintained at 37°C with 5% CO2 in Dulbecco's Modified Eagle's Medium (DMEM; Welgene), supplemented with 10% heat-

353 inactivated fetal bovine serum (FBS), HEPES, non-essential amino-acids, L-glutamine and 1X
354 Antibiotic-Antimycotic solution (Gibco). iPSC (SPC2 iPSC line, clone SPC2-ST-B2, Boston
355 University) derived alveolar epithelial type 2 cells (iAEC2s) were differentiated as previously
356 described and maintained as alveolospheres embedded in 3D Matrigel in "CK+DCI" media, as
357 previously described (Jacob et al. 2019). iAEC2s were passaged approximately every two weeks
358 by dissociation into single cells via the sequential application of dispase (2mg/ml, Thermo Fisher
359 Scientific, 17105-04) and 0.05% trypsin (Invitrogen, 25300054) and re-plated at a density of 400
360 cells/µl of Matrigel (Corning, 356231), as previously described (Jacob et al. 2019). SARS-CoV-2
361 WA1 strain was obtained by BEI resources and was propagated in Vero E6 cells. Viral titers were
362 determined by TCID50 assays in Vero E6 cells (Reed and Muench method) by microscopic
363 scoring. All experiments using SARS-CoV-2 were performed at the University of Michigan under
364 Biosafety Level 3 (BSL3) protocols in compliance with containment procedures in laboratories
365 approved for use by the University of Michigan Institutional Biosafety Committee (IBC) and
366 Environment, Health and Safety (EHS).

367

368 **Viral titer determination.** Vero E6, Caco-2 and Huh7 cells were seeded in a 48-well plate at
369 2x10^4 cells/well incubated overnight at 37°C with 5% CO2. Cells were then infected with SARS-
370 CoV-2 WA1 at a multiplicity of infection (MOI) of 0.2. One hour after infection, cells were harvested
371 (day 0 of infection) or kept at 37°C for 1, 2 and 3 days p.i. Viral titer determination was performed
372 by TCID50 assay on Vero E6 cells of the total virus (supernatant and intracellular fraction).
373 Alternatively, cells were harvested with Trizol and total cellular and viral RNA was extracted with
374 the ZymoGen Direct-zol RNA extraction kit. Viral RNA was quantified by RT-qPCR using the
375 2019-nCoV CDC qPCR Probe Assay and the probe set N1 (IDT technologies). IFNβ, viperin, MX1,
376 ISG15, IFITM3 and the housekeeping gene GAPDH mRNA levels were quantified by qPCR with
377 SsoAdvanced™ Universal SYBR® Green Supermix (Bio-Rad) with specific primers (IFNβ: F-

378 TTGACATCCCTGAGGAGATTAAGC, R- TCCCACGTACTCCAACTTCCA; MX1: F-
379 CCAGCTGCTGCATCCCACCC, R-AGGGGCGCACCTT CTCCTCA; ISG15: F-
380 TGGCGGGCAACGAATT, R- GGGTGATCTGCGCCTTCA; IFITM3: F-TCCCAC
381 GTACTCCAACTTCCA, R-AGCACCAGAAACACGTGCACT; GAPDH: F-
382 CTCTGCTCCTCCTGTTCGAC, R-GCGCCCCACCAAGCTCAAGA). Fold increase was
383 calculated by using the ΔΔCt method over non-infected untreated Huh7.

384 **Viral infectivity assay**. 384-well plates (Perkin Elmer, 6057300) were seeded with Huh7 cells at
385 3000 cells/well and allowed to adhere overnight. Compounds were then added to the cells and
386 incubated for 4 hours. The plates were then transferred to BSL3 containment and infected with
387 SARS-CoV-2 WA1 at a multiplicity of infection (MOI) of 0.2 in a 10 µL addition with shaking to
388 distribute virus. For the final dose-responses curves, porcine trypsin (Sigma-Aldrich, T0303) at a
389 final concentration of 2µg/ml was included during infection. After one hour of absorption, the virus
390 inoculum was removed, and media replaced with fresh compound. Uninfected cells and vehicle-
391 treated cells were included as positive and negative control, respectively. Two days post-infection,
392 cells were fixed with 4% PFA for 30 minutes at room temperature, permeabilized with 0.3% Triton
393 X-100 and blocked with antibody buffer (1.5% BSA, 1% goat serum and 0.0025% Tween 20). The
394 plates were then sealed, surface decontaminated, and transferred to BSL2 for staining with the
395 optimized fluorescent dye-set: anti-nucleocapsid protein (anti-NP) SARS-CoV-2 antibody
396 (Antibodies Online, Cat# ABIN6952432) overnight treatment at 4C followed by staining with
397 secondary antibody Alexa-647 (goat anti-mouse, Thermo Fisher, A21235), Hoechst-33342
398 pentahydrate (bis-benzimide) for nuclei staining (Thermo FIsher, H1398), HCS LipidTOX™ Green
399 Neutral Lipid Stain (Thermo Fisher, H34475), and HCS CellMask™ Orange for cell delineation
400 (Thermo Fisher H32713). iAEC2 maintained in 3D culture were dissociated to single cells and
401 seeded in collagen coated 384-well plates at a seeding density of 8000 cells/well in the presence
402 of 10 µM Y-27632 for the first 72 hours after plating (APExBIO, A3008 to grow to roughly 80%

403 confluence. Infection was performed at MOI of 10 in the presence of 2μg/ml of trypsin porcine
404 (Sigma-Aldrich, T0303). Staining protocol for the iAEC2s differed slightly with the addition of an
405 anti-acetylated tubulin primary antibody (Cell Signaling, 5335), instead of HCS CellMask Orange,
406 and the use of an additional secondary Alexa 488 antibody (donkey anti-rabbit, Jackson
407 ImmunoResearch, 711-545-152).

408 **Viral Binding assay**

409 Huh-7 cells were plated in 48-well plates at 100,000 cells per well and allowed to adhere
410 overnight. The following day, compounds were added at the indicated concentration in serum-
411 free DMEM and incubated for 1 hour at 4℃. Following compound incubation, cells were infected
412 with SARS-CoV-2 at an MOI of 10 for 1 hour at 4℃ to allow for viral binding. Cells were then
413 washed 3 times with ice cold PBS to remove unbound virus and RNA was extracted by using
414 the Direct-Zol RNA miniprep kit (Zymogen, R2052). Bound virus was then quantified by RT-
415 qPCR (see section Viral titer determination and host gene quantification) and percentages were
416 calculated over the Infected non-treated condition.

417 **Multi-cycle cytopathogenic effect (CPE) reduction assay.** Vero E6 were allowed to adhere
418 overnight in 96-well cell culture plates. A 1:2 10-point serial dilution of compounds (5000nM-5nM)
419 and SARS-CoV-2 at MOI of 0.002 were added. CPE was evaluated by microscopic scoring at
420 5dpi. The 50% inhibitory concentration (IC50) was calculated by logarithmic interpolation and is
421 defined as the concentration at which the virus-induced CPE is reduced by 50%.

422

423 **Compound library**. The compound library deployed for drug screening was created using the
424 FDA-Approved Drugs Screening Library (Item No. 23538) from Cayman Chemical Company. This
425 library of 875 compounds was supplemented with additional FDA approved drugs and rationally
426 included clinical candidates from other vendors including MedChemExpress, Sigma Aldrich, and

427 Tocris. Our library was formatted in five 384-well compound plates and was dissolved in DMSO
428 at 10 mM. Hololactoferrin (Sigma Aldrich, L4765), apolactoferrin (Jarrow Formulas, 121011),
429 native human lactoferrin (Creative BioMart, LFT-8196H) and transferrin (Sigma Aldrich, T2036)
430 were handled separately and added manually in cell culture media. Dilution plates were generated
431 for qHTS at concentrations of 2 mM, 1 mM, 500 μM, 250 μM and 50 μM and compounds were
432 dispensed at 1:1000 dilution.

433

434 **qHTS primary screen and dose response confirmation**. For the qHTS screen, compounds
435 were added to cells using a 50 nL pin tool Caliper Life Sciences Sciclone ALH 3000 Advanced
436 Liquid Handling system at the University of Michigan Center for Chemical Genomics (CCG).
437 Concentrations of 2 μM, 1 μM, 500 nM, 250 nM and 50 nM were included for the primary screen.
438 Post qHTS screen, all compounds were dispensed using an HP D300e Digital Compound
439 Dispenser and normalized to a final DMSO concentration of 0.1% DMSO. Confirmation dose
440 response was performed in triplicate and in 10-point:2-fold dilution.

441

442 **Imaging**. Stained cell plates were imaged on both Yokogawa CQ1 and Thermo Fisher CX5 high
443 content microscopes with a 20X/0.45NA LUCPlan FLN objective. Yokogawa CQ1 imaging was
444 performed with four excitation laser lines (405nm/488nm/561nm/640nm) with spinning disc
445 confocal and 100ms exposure times. Laser power was adjusted to yield optimal signal to noise
446 ratio for each channel. Maximum intensity projection images were collected from 5 confocal
447 planes with a 3-micron step size. Laser autofocus was performed and nine fields per well were
448 imaged covering approximately 80% of the well area. The Thermofisher CX5 with LED excitation
449 (386/23nm, 485/20nm, 560/25nm, 650/13nm) was also used and exposure times were optimized
450 to maximize signal/background. Nine fields were collected at a single Z-plane as determined by

image-based autofocus on the Hoechst channel. The primary qHTS screen was performed using CX5 images and all dose-response plates were imaged using the CQ1.

Image segmentation and feature extraction. The open source CellProfiler software was used in an Ubuntu Linux-based distributed Amazon AWS cloud implementation for segmentation, feature extraction and results were written to an Amazon RDS relational database using MySQL. A pipeline was developed to automatically identify the nuclei, cell, cytoplasm, nucleoli, neutral lipid droplets and syncytia for feature extraction. Multiple intensity features and radial distributions were measured for each object in each channel and cell size and shape features were measured. Nuclei were segmented using the Hoechst-33342 image and the whole cell mask was generated by expanding the nuclear mask to the edge of the Cell Mask Orange image.

Data pre-processing. Cell level data were pre-processed and analyzed in the open source Knime analytics platform[48]. Cell-level data was imported into Knime from MySQL, drug treatment metadata was joined, and features were centered and scaled. Features were pruned for low variance (<5%) and high correlation (>95%) and resulted in 660 features per cell.

Statistical methods and hypothesis testing. Dose-response curves were fit and pairwise differences between experimental conditions were tested using Prism (Graphpad Software, San Diego, CA, USA). Other statistical tests were performed in the statistical programming language and environment R.

Machine learning - infectivity score and field-level scoring. Multiple logistic regression as implemented in the statistical language and environment R was used to identify features characteristic of cells within infected wells. Models were fit to cells from infected and uninfected control wells in the first five plate-series of the quantitative high throughput screen. As an independent benchmark, these logistic regression models were validated against a manually selected set of individual infected and uninfected cells; features which degraded performance on the benchmark were excluded from the model. The final model included only virus channel intensity features in the cell and cytoplasm ROIs. As a threshold for initial classification, the minimum value from virus-infected cells in the benchmark was used; the final decision rule is given in Eq. 1.

(Eq.1) : A cell is infected if (Cells_Intensity_IntegratedIntensityEdge_Virus × 0.1487025 + Cells_Intensity_MeanIntensityEdge_Virus × -38.40196 + Cells_Intensity_MaxIntensityEdge_Virus × 42.70269 + Cytoplasm_Intensity_StdIntensity_Virus × 42.54849) ≥ 1.525285

Then, individual field images from the infected control were categorized as confirmed-infected when the mean feature values, across all cells in the field, were above the threshold in Eq. 1. Using mean values for all 660 cell-profiler features in each field, a random forest classifier was trained to predict a probability of membership in the category of uninfected control fields vs confirmed-infected fields. The output of this random forest classifier is reported as “Probpos” (for the positive, uninfected control), throughout. Field level mean/median feature values were computed and a random forest model was fit between the positive control (32

496 uninfected wells) and the negative control (32 infected wells, 0.1% DMSO vehicle treated)
497 with 80/20 cross validation. The compound treated wells were scored with the RF model and
498 the efficacy score was normalized to the individual plate.

499

500 **UMAP embedding**. The embed_umap application of MPLearn (v0.1.0,
501 https://github.com/momeara/MPLearn) was used to generate UMAP embeddings. Briefly, each
502 for a set of cells, each feature was per-plate standardized and jointly orthogonalized using
503 sklearn.IncrementalPCA(n_components=379, batch_size=1000). Then features were embedded
504 into 2-dimensions using umap-learn (v0.4.1)[12] with umap. UMAP(n_components=2,
505 n_neighbors=15, min_dist=0, init='spectral', low_memory=True). Embeddings were visualized
506 using Holovies Datashader (v1.12.7)[49], using histogram equalization and the viridis color map.
507 Visualizing subsets was done in JMP Pro 14.

508

509 **Data analytics**. HC Stratominer (Core Life Analytics, Utrecht NL) was used as an independent
510 method for hit-calling and performs fully automated/streamlined cell-level data pre-processing and
511 score generation. IC Stratominer was also used to fit dose response curves for qHTS.
512 Compound registration and assay data registration were performed using the open source
513 ACAS platform (Refactor BioSciences github https://github.com/RefactorBio/acas).

514

515 **Dose-response analysis and compound selection.** In qHTS screening, a compound was
516 selected to be carried forward into full dose response confirmation when meeting one of the
517 following criteria: 1) Probpos greater than 0.75 for the median field in at least three concentrations,
518 with per-field cell counts at least 60% of the positive control, and without an observed standard

519 deviation in Probpos across-fields-in-the-well of 0.4 or greater, 2) a dose-response relationship
520 with Probpos was observed (by inspection) across the five concentrations tested, including
521 compounds with Propbos greater than 0.90 at the two highest concentrations, or 3) compounds
522 of interest not meeting this criteria were carried forward if reported positive in the literature or were
523 being evaluated in clinical trials for COVID-19.

524

525 **Dose response analysis in the confirmation and combinatorial screening.** Due to the spatial
526 inhomogeneity of infected cells across a single well, approximately half of the fields were
527 undersaturated, leading to a consistent distribution in Probpos that saturates in the top third of 27
528 rank-ordered fields (from 9 fields and triplicate wells) for each concentration tested. The Probpos
529 effect for a compound concentration was tabulated by averaging the top third of rank ordered
530 fields. Outlier fields with high Probpos values were visually inspected and eliminated if artifacts
531 (segmentation errors or debris) were observed. Cells treated with known fluorescence drugs
532 including Clofazimine, were confirmed to not have spectral interference. Dose response curves
533 were fit with Graphpad Prism using a semilog 4-parameter variable slope model.

534

535

536

537

538

539

540

541

542

543

FIGURES AND LEGENDS

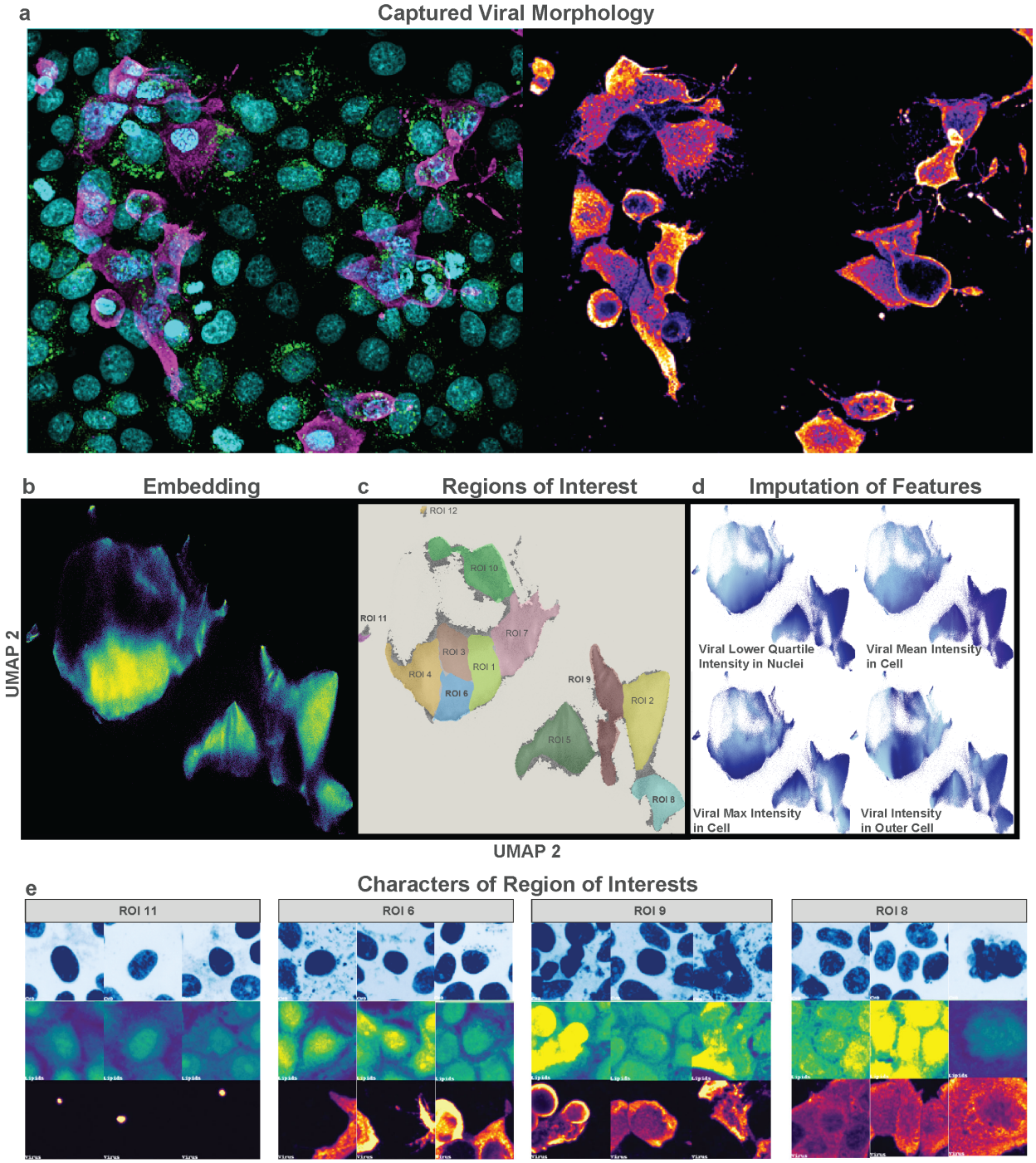

Figure 1. Morphological profiling of SARS-CoV-2 infected Huh7 cells (MOI of 0.2 for 48 hrs). a) representative field (left) with nuclei (cyan), neutral lipids (green), and SARS-CoV-2 NP (magenta) and the NP image in the same area with “fire” false color LUT showing distinct morphologies of infected cells showing small/round cells with a hollow center, cells with protrusions, and large syncytia. Representative image was acquired on a Yokogawa CQ1 high-content imager at with a 60X lens and visualized with Fiji ImageJ. b) 2 dimensional UMAP embedding of 2.47 million infected cells using 379 morphological features. c) Cluster regions of

554 interest (ROI) in the UMAP are highlighted. d) UMAP projection colored by NP viral staining
555 intensity for four measurements where viral measurements with darker blue representing
556 greater value in those regions. e) For four ROIs, a representative cell is shown for the nuclear
557 (top), CellMask(middle), and SARS-CoV-2 NP channels (bottom).
558

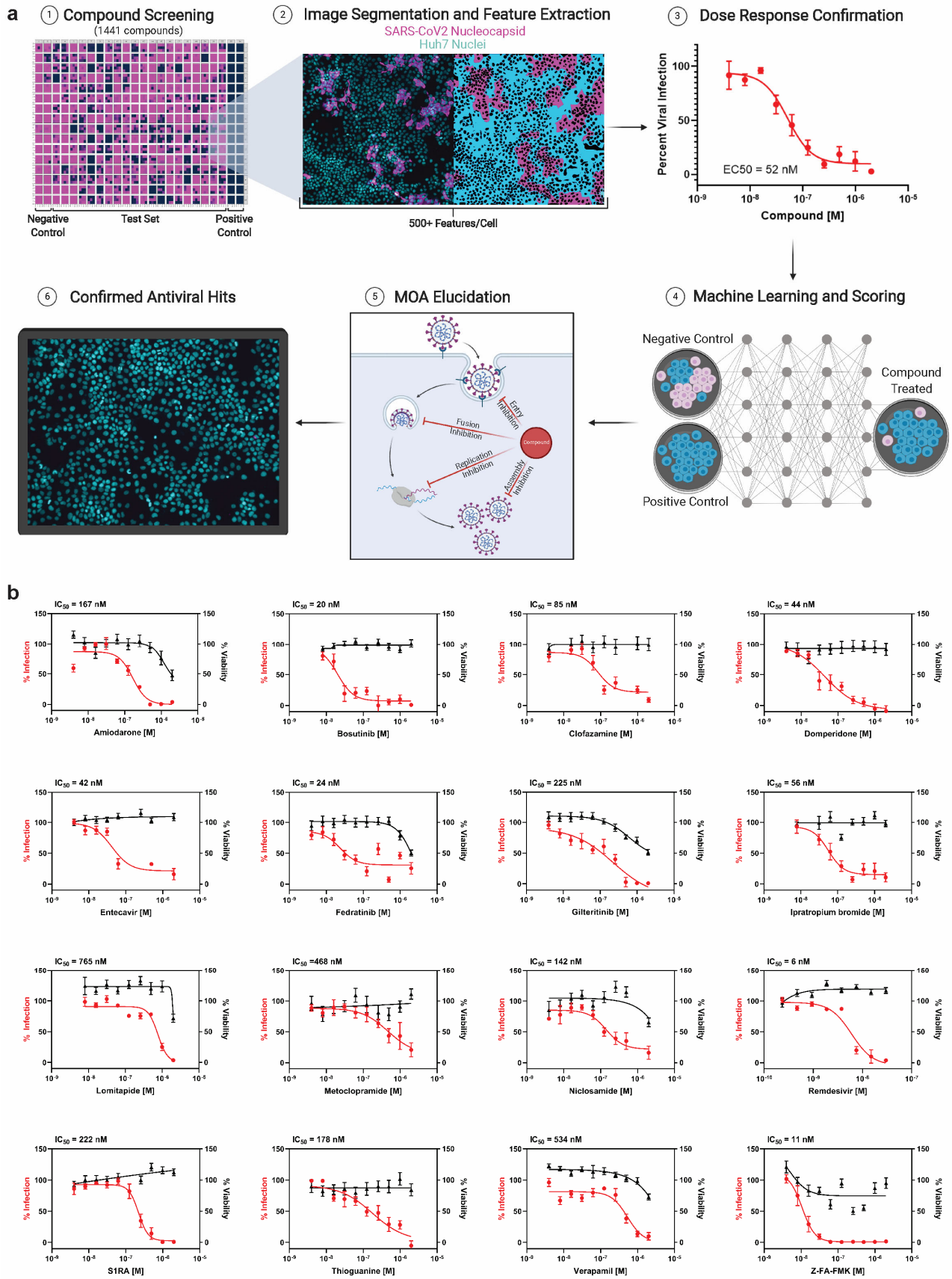
a
1 Compound Screening
(1441 compounds)
Negative Control
Test Set
Positive Control
2 Image Segmentation and Feature Extraction
SARS-CoV2 Nucleocapsid
Huh7 Nuclei
500+ Features/Cell
3 Dose Response Confirmation
Percent Viral Infection
EC50 = 52 nM
Compound [M]
4 Machine Learning and Scoring
Negative Control
Compound Treated
Positive Control
5 MOA Elucidation
Entry Inhibition
Fusion Inhibition
Compound
Replication Inhibition
Assembly Inhibition
6 Confirmed Antiviral Hits
b
IC50 = 167 nM
Amiodarone [M]
IC50 = 20 nM
Bosutinib [M]
IC50 = 85 nM
Clofazamine [M]
IC50 = 44 nM
Domperidone [M]
IC50 = 42 nM
Entecavir [M]
IC50 = 24 nM
Fedratinib [M]
IC50 = 225 nM
Gilteritinib [M]
IC50 = 56 nM
Ipratropium bromide [M]
IC50 = 765 nM
Lomitapide [M]
IC50 =468 nM
Metoclopramide [M]
IC50 = 142 nM
Niclosamide [M]
IC50 = 6 nM
Remdesivir [M]
IC50 = 222 nM
S1RA [M]
IC50 = 178 nM
Thioguanine [M]
IC50 = 534 nM
Verapamil [M]
IC50 = 11 nM
Z-FA-FMK [M]
% Infection
% Viability

559

Figure 2. a) Schematic representation of the anti-SARS-CoV-2 therapy discovery effort. 1) Compounds are administered to cells cultured on 384-well plates infected with SARS-CoV-2. Each plate contains 24 negative (infected) and 24 positive (non-infected) control wells to adjust for plate-to-plate variation. 2) Cells are fixed, stained, and imaged. Images are analyzed through a Cell Profiler-based pipeline which segments nuclei, cell boundaries, neutral lipid content and viral syncytia formation while extracting features of these cellular compartments. 3) Dose-response curves are calculated through multivariate-analysis to define per-image viral infectivity 4) Machine learning models are built around positive and negative control wells based on extracted features and applied to each drug condition. 5) Models inform on individual compound mode(s) of antiviral action through obtained features 6) confirmed antiviral hits; b) Dose-response curves of 16 hits of the drug screening. Graphs represent median SEM of 10-point 1:2 dilution series of selected compounds for N=3 biological replicates. IC50 were calculated based on normalization to the control and after fitting in GraphPad Prism.

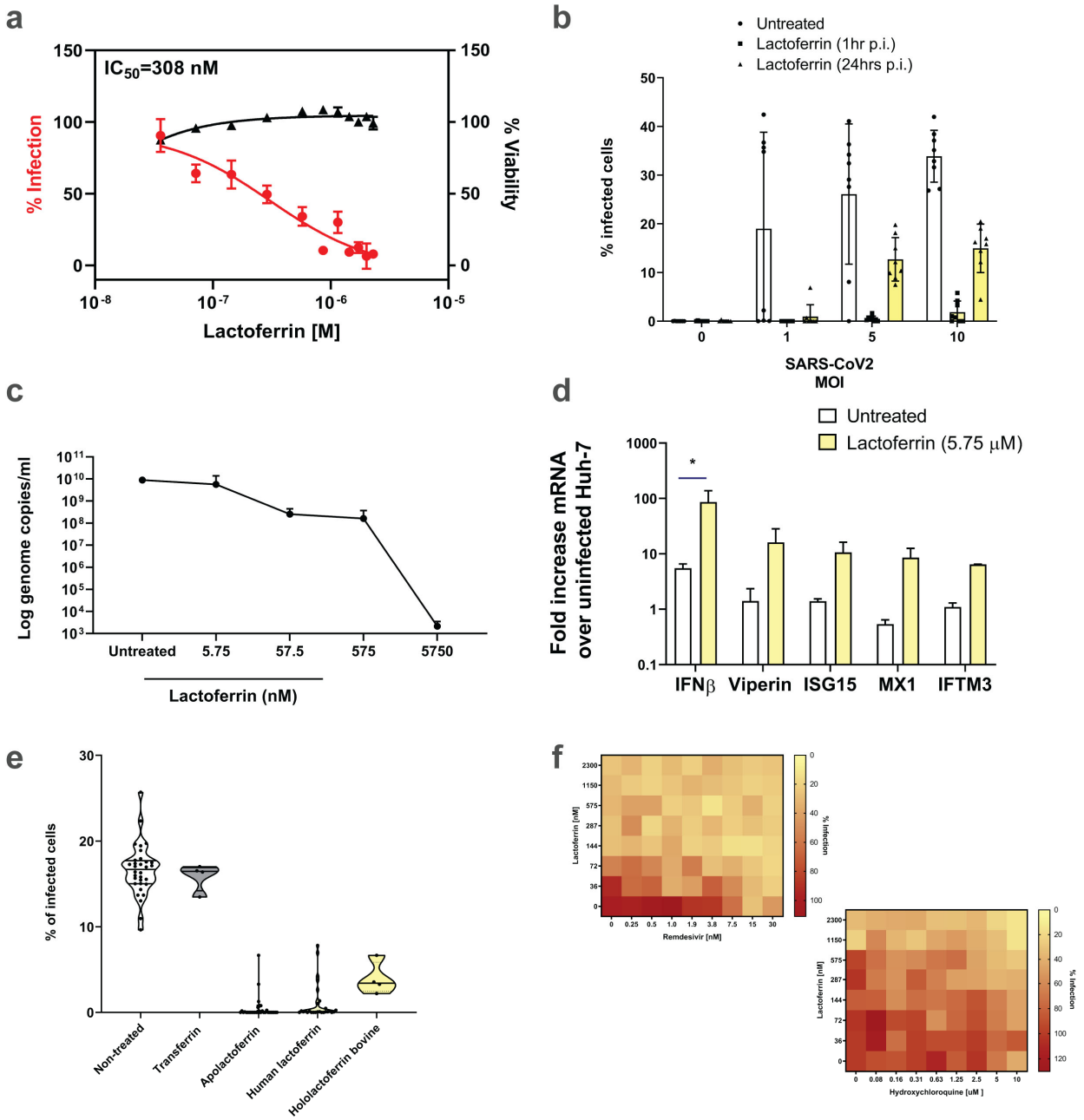

Figure 3. Lactoferrin blocks SARS-CoV-2 replication at different stages of the viral cycle. a) Huh7 cells were treated with lactoferrin (0 to 2.3 μM) and infected with SARS-CoV-2 (MOI of 0.2) in a 384-well plate. Plates were imaged using automated fluorescence microscopy and processed using our image analysis pipeline to determine percent viral inhibition. Graph indicates a dose-response (RED, IC50 = 308 μM). Cell viability is depicted in black. b) Huh7 were infected with SARS-CoV-2 (MOI of 1, 5 and 10; MOI of 0 indicates non-infected cells) and treated with 2.3 μM of lactoferrin at 1 and 24 hrs p.i. Bars indicate the percentage of infected cells in different conditions. Data is an average of eight replicates. Statistical significance determined using multiple student's t-test with the Bonferroni-Dunn method, with alpha = 0.05. Except for MOI of 0, all conditions (Untreated vs Lactoferrin, 1 hr or Untreated vs Lactoferrin, 24 hr) differ at P<0.0001. c-d) 2.5x104 Huh7 cells were infected with SARS-CoV-2 at MOI of 0.2.

587 48 hrs p.i., cells were harvested and RNA was extracted. Viral genome copies were calculated
588 with an absolute quantification method (standard curve) (c) and mRNA levels of cellular IFNβ,
589 MX1, ISG15 and IFITM3 (d) were calculated with ΔΔCt over non-infected Huh7. Data are
590 average, SD of N=2 biological replicates with n=3 technical replicates each. Statistical
591 significance determined using multiple student's t-test with the Bonferroni-Dunn method, with
592 alpha = 0.05. *P<0.001. e) Percentage of SARS-CoV-2 infected Huh7 cells upon treatment with
593 bovine apolactoferrin and hololactoferrin, native human lactoferrin and transferrin at a
594 concentration of 2.3 μM. f) 2-dimensional dose response heat maps of lactoferrin (0 to 2.3 μM)
595 in combination with remdesivir and hydroxychloroquine (0 to 30 nM and 0 to 10 μM,
596 respectively). Remdesivir combination was evaluated with a 0.2 MOI and HCQ was evaluated
597 with a MOI of 10 leading to a relative shift in lactoferrin
598 potency.

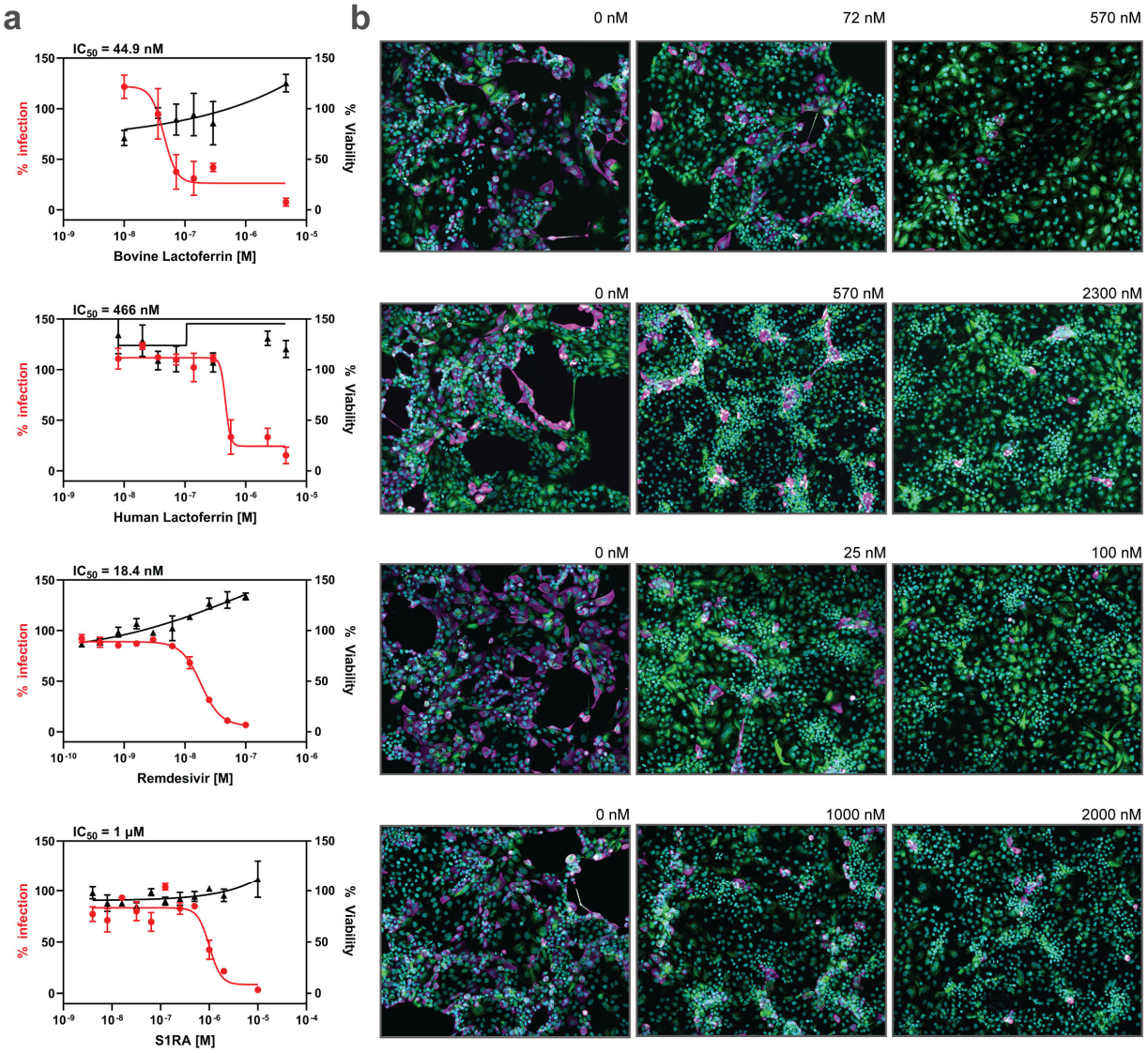

599
600 Figure 4. Antiviral activity of selected compounds was assessed in iAEC2 cells infected with
601 SARS-CoV-2 at MOI 10. Bovine and human lactoferrin exhibited IC50 of 44.9 and 466 nM
602 respectively. Remdesivir and S1RA exhibited IC50 of 18.4 nM and 1 μM respectively. Images of
603 nuclei (cyan), acetylated tubulin (green), and NP (magenta) from non-treated infected control,
604 IC50, and ICmax.

605 **SUPPLEMENTARY INFORMATION**

606 Supplementary Figure 1: Growth kinetics for VeroE6, Huh7 and Caco-2 cells.
607 Supplementary Figure 2: Summary measurements for UMAP ROIs in Figure 1.
608 Supplementary Figure 3: Drugs that exacerbate SARS-CoV-2 infection in vitro.
609 Supplementary Figure 4: Viral entry inhibition for lactoferrin.
610 Supplementary Figure 5: Synergy in efficacy for remdesivir/hydroxychloroquine with lactoferrin.
611 Supplementary Figure 6: Dose response of drugs in iAEC2 at MOI=0.2.
612 Supplementary Table 1: Compound Deep Dives
613 Supplementary File 1: Compound library details
614 Supplementary File 2: 3D reconstruction video of infected cells
615

616 **REFERENCES**

617 1. Xiao, F. *et al.* Evidence for Gastrointestinal Infection of SARS-CoV-2. *Gastroenterology*
618 (2020) doi:10.1053/j.gastro.2020.02.055.

619 2. Lin, L. *et al.* Gastrointestinal symptoms of 95 cases with SARS-CoV-2 infection. *Gut*
620 (2020) doi:10.1136/gutjnl-2020-321013.

621 3. Avula, A. *et al.* COVID-19 presenting as stroke. *Brain. Behav. Immun.* (2020)
622 doi:10.1016/j.bbi.2020.04.077.

623 4. Kochi, A. N., Tagliari, A. P., Forleo, G. B., Fassini, G. M. & Tondo, C. Cardiac and
624 arrhythmic complications in patients with COVID-19. *Journal of Cardiovascular*
625 *Electrophysiology* (2020) doi:10.1111/jce.14479.

626 5. Mulangu, S. *et al.* A randomized, controlled trial of Ebola virus disease therapeutics. *N.*
627 *Engl. J. Med.* (2019) doi:10.1056/NEJMoa1910993.

628 6. Oprea, T. I. *et al.* Drug repurposing from an academic perspective. *Drug Discovery*
629 *Today: Therapeutic Strategies* (2011) doi:10.1016/j.ddstr.2011.10.002.

630 7. Chu, H. *et al.* Comparative tropism, replication kinetics, and cell damage profiling of
631 SARS-CoV-2 and SARS-CoV with implications for clinical manifestations, transmissibility,
632 and laboratory studies of COVID-19: an observational study. *The Lancet Microbe* (2020)
633 doi:10.1016/s2666-5247(20)30004-5.

634 8. Hoffmann, M. *et al.* SARS-CoV-2 Cell Entry Depends on ACE2 and TMPRSS2 and Is

635 Blocked by a Clinically Proven Protease Inhibitor. *Cell* (2020)
636 doi:10.1016/j.cell.2020.02.052.
637 9. Gordon, D. E. *et al.* A SARS-CoV-2 protein interaction map reveals targets for drug
638 repurposing. *Nature* (2020) doi:10.1038/s41586-020-2286-9.
639 10. McQuin, C. *et al.* CellProfiler 3.0: Next-generation image processing for biology. *PLoS*
640 *Biol.* (2018) doi:10.1371/journal.pbio.2005970.
641 11. McInnes, L., Healy, J., Saul, N. & Großberger, L. UMAP: Uniform Manifold Approximation
642 and Projection. *J. Open Source Softw.* (2018) doi:10.21105/joss.00861.
643 12. Riva, L. *et al.* A Large-scale Drug Repositioning Survey for SARS-CoV-2 Antivirals.
644 *bioRxiv* (2020) doi:10.1101/2020.04.16.044016.
645 13. Katie Heiser *et al.* Identification of potential treatments for COVID-19 through artificial
646 intelligence enabled phenomic analysis of human cells infected with SARS-CoV-2.
647 *bioRxiv* (2020) doi:10.1101/2020.04.21.054387.
648 14. Jeon, S. *et al.* Identification of antiviral drug candidates against SARS-CoV-2 from FDA-
649 approved drugs. *Antimicrob. Agents Chemother.* (2020) doi:10.1128/AAC.00819-20.
650 15. Lang, J. *et al.* Inhibition of SARS pseudovirus cell entry by lactoferrin binding to heparan
651 sulfate proteoglycans. *PLoS One* (2011) doi:10.1371/journal.pone.0023710.
652 16. Kell, D. B., Heyden, E. L. & Pretorius, E. The Biology of Lactoferrin, an Iron-Binding
653 Protein That Can Help Defend Against Viruses and Bacteria. *Front. Immunol.* (2020)
654 doi:10.3389/fimmu.2020.01221.
655 17. Siqueiros-Cendón, T. *et al.* Immunomodulatory effects of lactoferrin. *Acta*
656 *Pharmacologica Sinica* (2014) doi:10.1038/aps.2013.200.
657 18. Yeni, P. Update on HAART in HIV. in *Journal of Hepatology* (2006).
658 doi:10.1016/j.jhep.2005.11.021.
659 19. Hurley, K. *et al.* Reconstructed Single-Cell Fate Trajectories Define Lineage Plasticity
660 Windows during Differentiation of Human PSC-Derived Distal Lung Progenitors. *Cell*

661 *Stem Cell* (2020) doi:10.1016/j.stem.2019.12.009.
662 20. Jacob, A. *et al.* Derivation of self-renewing lung alveolar epithelial type II cells from
663 human pluripotent stem cells. *Nat. Protoc.* (2019) doi:10.1038/s41596-019-0220-0.
664 21. Mason, R. J. Pathogenesis of COVID-19 from a cell biology perspective. *European*
665 *Respiratory Journal* (2020) doi:10.1183/13993003.00607-2020.
666 22. Hibbs, A. M. & Lorch, S. A. Metoclopramide for the treatment of gastroesophageal reflux
667 disease in infants: A systematic review. *Pediatrics* (2006) doi:10.1542/peds.2005-2664.
668 23. Hajifathalian, K. *et al.* SARS-COV-2 infection (coronavirus disease 2019) for the
669 gastrointestinal consultant. *World J. Gastroenterol.* (2020) doi:10.3748/wjg.v26.i14.1546.
670 24. Roscow, O., Ganassin, R., Garver, K. & Polinski, M. Z-FA-FMK demonstrates differential
671 inhibition of aquatic orthoreovirus (PRV), aquareovirus (CSRV), and rhabdovirus (IHNV)
672 replication. *Virus Res.* (2018) doi:10.1016/j.virusres.2017.11.024.
673 25. Ou, X. *et al.* Characterization of spike glycoprotein of SARS-CoV-2 on virus entry and its
674 immune cross-reactivity with SARS-CoV. *Nat. Commun.* (2020) doi:10.1038/s41467-020-
675 15562-9.
676 26. Pardanani, A. *et al.* TG101209, a small molecule JAK2-selective kinase inhibitor potently
677 inhibits myeloproliferative disorder-associated JAK2V617F and MPLW515L/K mutations.
678 *Leukemia* (2007) doi:10.1038/sj.leu.2404750.
679 27. Wu, D. & Yang, X. O. TH17 responses in cytokine storm of COVID-19: An emerging
680 target of JAK2 inhibitor Fedratinib. *J. Microbiol. Immunol. Infect.* (2020)
681 doi:10.1016/j.jmii.2020.03.005.
682 28. Zhang, W. *et al.* The use of anti-inflammatory drugs in the treatment of people with
683 severe coronavirus disease 2019 (COVID-19): The experience of clinical immunologists
684 from China. *Clinical Immunology* (2020) doi:10.1016/j.clim.2020.108393.
685 29. Stebbing, J. *et al.* COVID-19: combining antiviral and anti-inflammatory treatments. *The*
686 *Lancet Infectious Diseases* (2020) doi:10.1016/S1473-3099(20)30132-8.

687 30. Treatment of Moderate to Severe Coronavirus Disease (COVID-19) in Hospitalized
688 Patients. (2020).
689 31. Delprat, B., Crouzier, L., Su, T. P. & Maurice, T. At the Crossing of ER Stress and MAMs:
690 A Key Role of Sigma-1 Receptor? in *Advances in Experimental Medicine and Biology*
691 (2020). doi:10.1007/978-3-030-12457-1_28.
692 32. Friesland, M., Mingorance, L., Chung, J., Chisari, F. V. & Gastaminza, P. Sigma-1
693 Receptor Regulates Early Steps of Viral RNA Replication at the Onset of Hepatitis C
694 Virus Infection. *J. Virol.* (2013) doi:10.1128/jvi.03557-12.
695 33. Fung, T. S. & Liu, D. X. Coronavirus infection, ER stress, apoptosis and innate immunity.
696 *Frontiers in Microbiology* (2014) doi:10.3389/fmicb.2014.00296.
697 34. Moebius, F. F., Reiter, R. J., Hanner, M. & Glossmann, H. High affinity of sigma1-binding
698 sites for sterol isomerization inhibitors: Evidence for a pharmacological relationship with
699 the yeast sterol C8-C7 isomerase. *Br. J. Pharmacol.* (1997) doi:10.1038/sj.bjp.0701079.
700 35. Díaz, J. L. *et al.* Synthesis and biological evaluation of the 1-arylpyrazole class of σ1
701 receptor antagonists: Identification of 4-{2-[5-methyl-1- (naphthalen-2-yl)-1H-pyrazol-3-
702 yloxy]ethyl}morpholine (S1RA, E-52862). *J. Med. Chem.* (2012) doi:10.1021/jm3007323.
703 36. Torres, V. *et al.* QT prolongation and the antiarrhythmic efficacy of amiodarone. *J. Am.*
704 *Coll. Cardiol.* (1986) doi:10.1016/S0735-1097(86)80272-8.
705 37. Vidal-Torres, A. *et al.* Effects of the selective sigma-1 receptor antagonist S1RA on
706 formalin-induced pain behavior and neurotransmitter release in the spinal cord in rats. *J.*
707 *Neurochem.* (2014) doi:10.1111/jnc.12648.
708 38. Gris, G. *et al.* The selective sigma-1 receptor antagonist E-52862 attenuates neuropathic
709 pain of different aetiology in rats. *Sci. Rep.* (2016) doi:10.1038/srep24591.
710 39. Reghunathan, R. *et al.* Expression profile of immune response genes in patients with
711 severe acute respiratory syndrome. *BMC Immunol.* (2005) doi:10.1186/1471-2172-6-2.
712 40. Cutone, A. *et al.* Lactoferrin prevents LPS-induced decrease of the iron exporter

713 ferroportin in human monocytes/macrophages. *BioMetals* (2014) doi:10.1007/s10534-
714 014-9742-7.
715 41. Conti, P. *et al.* Induction of pro-inflammatory cytokines (IL-1 and IL-6) and lung
716 inflammation by COVID-19: anti-inflammatory strategies. *Journal of biological regulators*
717 *and homeostatic agents* (2020) doi:10.23812/CONTI-E.
718 42. Lagunas-Rangel, F. A. & Chávez-Valencia, V. High IL-6/IFN-γ ratio could be associated
719 with severe disease in COVID-19 patients. *Journal of Medical Virology* (2020)
720 doi:10.1002/jmv.25900.
721 43. Han, C. *et al.* Digestive Symptoms in COVID-19 Patients With Mild Disease Severity:
722 Clinical Presentation, Stool Viral RNA Testing, and Outcomes. *Am. J. Gastroenterol.*
723 (2020) doi:10.14309/ajg.0000000000000664.
724 44. Oda, H. *et al.* Antiviral Effects of Bovine Lactoferrin on Human Norovirus. *Biochem. Cell*
725 *Biol.* (2020) doi:10.1139/bcb-2020-0035.
726 45. Mohamed, J. A. *et al.* A Novel Single-Nucleotide Polymorphism in the Lactoferrin Gene Is
727 Associated with Susceptibility to Diarrhea in North American Travelers to Mexico. *Clin.*
728 *Infect. Dis.* (2007) doi:10.1086/512199.
729 46. Gu, J., Han, B. & Wang, J. COVID-19: Gastrointestinal Manifestations and Potential
730 Fecal–Oral Transmission. *Gastroenterology* (2020) doi:10.1053/j.gastro.2020.02.054.
731 47. Hung, I. F.-N. *et al.* Triple combination of interferon beta-1b, lopinavir–ritonavir, and
732 ribavirin in the treatment of patients admitted to hospital with COVID-19: an open-label,
733 randomised, phase 2 trial. *Lancet* (2020) doi:10.1016/s0140-6736(20)31042-4.
734 48. Berthold, M. R. *et al.* KNIME: The konstanz information miner. in *4th International*
735 *Industrial Simulation Conference 2006, ISC 2006* (2006). doi:10.1007/978-3-540-78246-
736 9_38.
737 49. Stevens, J.-L., Rudiger, P. & Bednar, J. HoloViews: Building Complex Visualizations
738 Easily for Reproducible Science. in *Proceedings of the 14th Python in Science*

Conference (2015). doi:10.25080/majora-7b98e3ed-00a.